Chapter 8
Fractal Analysis of the Pore Space in Sandstones as Derived from Mercury Porosimetry and Image Analysis

Grazyna Stanczak

Abstract The pore space fractal dimension was measured using a model of a porous body based on the Menger sponge and mercury porosimetry data for selected samples of the reservoir sandstones of the Weglowka oil field (SE Poland) in a pore-throat diameter range between 91 and 0.0090 μm. Based on the digital analyses of the two-dimensional images of thin sections impregnated with blue-dyed epoxy and taken under an optical microscope as well as the images of thin sections taken under a cold field emission gun scanning electron microscope (FEGSM) in the backscattered electron image mode, the current paper tries to quantify the pore space of sandstones by using the box counting method. The results derived from analysis of the pore-throat diameter distribution by mercury porosimetry revealed the multifractal structure of the pore space of sandstone in two separated ranges of the pore-throat size considerably lesser than the pore-throat diameters (10–50 μm) corresponding to threshold pressures. This means that only the pore throats connecting wider parts of the pore network (pores) exhibit the fractal structure. The assumption that the fractal dimension monitoring the distribution of the pore-space volume within the smallest pore-throat diameters characterizes the overall pore-throat network in the rock sample provides a device to set apart the distribution of the pore-throat volume from the distribution of the pore volume. On the other hand, the fractal dimensions derived from the image analysis of thin sections describe the pore space as a whole.

8.1 Introduction

The pore space of a sandstone is known as an extremely complicated, irregular system which can be considered as a chaotic structure with a high degree of heterogeneity. Owing to this complexity, it is very difficult to acquire a complete description of the

G. Stanczak (✉)
Faculty of Geology, Geophysics and Environmental Protection, AGH University of Science and Technology, al. Mickiewicza 30, 30-059, Krakow, Poland
e-mail: gstanczak@geol.agh.edu.pl

E. K. Polychroniadis et al. (eds.), *International Multidisciplinary Microscopy Congress*, Springer Proceedings in Physics 154, DOI: 10.1007/978-3-319-04639-6_8,

pore geometry. In order to obtain a quantitative characterization of this pore network, a number of approaches such as the mercury intrusion porosimetry and the image analysis of thin sections have been used for measuring structural parameters [2, 5, 16, 22, 27]. The application of the fractal geometry to describe properties of highly complex structures makes it possible to obtain extra information on the pore network using the fractal dimension, being a global measure of the roughness of the features [15] or of the surface irregularity, describing a heterogeneous surface with single numerical value [20]. The fractal nature of the pore system in sedimentary rocks such as sandstones has been reported by a number of authors [6, 8, 12–14, 24].

The author presents here the measurement of the pore space fractal dimensions, using two methodologies: the mercury intrusion porosimetry and the image analysis of thin sections. Samples included sandstones from outcrops of the Lower Cretaceous Lgota Beds located within the Weglowka fold, which is a structural trap for oil accumulations in the Weglowka oil field in the SE Poland (the Outer Carpathians).

The fractal geometry is used to describe the irregular and fragmented patterns which are characterized by their invariability at any scale of scrutiny (i.e. self-similarity) [15]. Its crucial purpose is to provide means by which seemingly chaotic and random systems can be quantified by fractal dimensions. The fractal dimensions in a multi-fractal pattern change at different levels of scrutiny, since different aspects of the pattern either become apparent or become no longer noticeable [7].

Complex structures observed in the nature reveal fractal properties (scale invariance) only in (i) a statistical sense and (ii) within a certain range of scale. It means that these fractal structures may exhibit a statistical distribution of objects which are more or less at random and if the number of objects N with a characteristic linear dimension greater than r satisfies the relation (i.e. a cumulative form of fractal relationship):

$$N = \frac{C}{r^D} \tag{8.1}$$

where C is a proportionality constant, r is a characteristic linear dimension, and D is the fractal dimension. Additionally, there is the range of scales, determined by a lower and upper limits, over which the scale invariance extends. These limits, called inner and outer cut-offs of the fractal regime, are not less important parameters than the fractal dimension (D) itself [21, 25, 26].

The Menger sponge used as a model for a porous medium is constructed from cubes of density ρ_0 and size r_0. It is assumed that each cube is solid and has no porosity [25, 26]. The first-order Menger sponge constructed from the zero-order cubes has the size $r_1 = 3^1 r_0$ and consists of 20 such cubes ($N_1 = 20^1$) so that the first-order density is $\rho_1 = 20\rho_0/27$. At the next smaller scale the size of the second-order sponge is $r_2 = 3^2 r_0$ and there are 400 ($N_2 = 20^2$) solid cubes of size r_0 with density ρ_0. Thus the density of the second-order Menger sponge is $\rho_2 = 400\rho_0/729$. The density of the nth-order Menger sponge is

$$\frac{\rho_n}{\rho_0} = \left(\frac{r_0}{r_n}\right)^{3-\frac{\ln 20}{\ln 3}} \tag{8.2}$$

This is a power-law relation, where the fractal dimension of the Menger sponge is $D = ln\ 20/\ln\ 3 = 2.727$. Thus for a fractal distribution of pore volume, the density of a rock increases with its size r according to

$$\frac{\rho}{\rho_0} = \left(\frac{r_0}{r}\right)^{3-D} \tag{8.3}$$

The density of a fractal solid systematically decreases with the increasing size of the sample considered [3, 25, 26].

8.2 Material and Methods

Samples and thin-section images. Four sandstone samples were selected for this study. They have a narrow range of densities (2.66–2.70 g/cm^3) determined with a helium pycnometer (Micromeritics Accypyc 1330). Porosities calculated using the densities and the data from mercury porosimeter vary widely from 9.55 to 28.42 % (Table 8.1). One polished thin section impregnated with blue-dyed epoxy was made per sample. All thin sections were examined with a standard optical microscope. Moreover, all of the samples were examined by scanning electron microscopy, using a Hitachi S-4700 FEGSM (a cold field emission gun scanning electron microscope) on other thin sections coated with coal. The field emission SEM was operated at an accelerating voltage of 20 kV and a working distance of 12.9–14.4 mm.

Image analysis. Images of the analyzed thin-sections were acquired with both the optical microscope (OM) by using the DS-Fi1 color camera (Nikon) and the FEGSM at backscatter imaging with an Autrata modified YAG crystal. The OM images were digitized as 1280×1024 24-bit color images covering an area of approximately $550 \times 440\,\mu$m for 10 ×-objective magnification. The FEGSM micrographs digitized as 2560×1920 8-bit gray-scale images cover an area of approximately $1150 \times 860\,\mu$m for 110 ×-magnification (length of scale 500 μm) or $976 \times 730\,\mu$m for 130 ×-objective magnification (length of scale 400 μm).

The original images acquired in this study were binarized into a pore phase and a solid phase using the Nikon's imaging software NIS-Elements BR (version 3.10). A simple *auto detect filled tool* using threshold technique allows a clear distinction between these two phases because of the high quality of the original images. The OM images were binarized by assigning pore phase to all pixels containing blue color tones. The FEGSM images have sufficient contrast to apply this tool to separate between dark pore space and light solid phase. The edges of the detected pore phase were smoothed by applying *a close transformation* with the 8-connectivity model. This procedure is performed as a dilation followed by erosion, resulting in smoothing of contours, filling of small holes and connecting very close objects (all pixels neighboring by the corner belong to one object). Continuously comparing the binarized image with the original thin-section image ensures the accuracy of the

Table 8.1 Density and effective porosity measured with proper device (pycnometer and porosimeter, respectively), and total porosity calculated for each sample. The box-counting fractal dimensions of the total optical porosity (TOP)

	Sample unit	1	2	3	4	Min	Max
Density	g/cm^3	2.70	2.70	2.67	2.66	2.66	2.70
Effective porosity	%	25.13	18.38	13.42	9.06	9.06	25.13
Total porosity	%	28.42	20.36	14.35	9.55	9.55	28.42
OM images							
D_{OM}		1.522	1.486	1.320	1.538	1.320	1.538
R^2		0.9953	0.9973	0.9968	0.9987	0.9953	0.9987
Total optical porosity	%	28.64	26.28	18.72	24.02	18.72	28.64
	μm^2	68,733.6	63,060.0	44,918.4	57,652.8	44,918.4	68,733.6
FEGSM images							
D_{FEGSM}		1.561	1.448	1.563	1.564	1.448	1.564
R^2		0.9991	0.9999	0.9996	0.9997	0.9991	0.9999
Total optical porosity	%	28.17	11.83	16.32	7.47	7.47	28.17
	μm^2	280,894.8	117,905.2	116,673.7	53,417.7	53,417.7	280,894.8

D_{OM}, D_{FEGSM}—the box-counting fractal dimension for the OM image and the FEGSM image, respectively; R^2—coefficient of determination

binarization process. For every studied sample two representative micrographs, the OM image and the FEGSM image, were chosen to image analysis.

The box-counting fractal dimension. Fractal dimension of pore space was determined with the box counting method performed on binary images. This method involve superimposing boxes with the box size δ onto the image and recording the number of boxes $N(\delta)$ covering the pore spaces. This process is repeated for different box sizes. If the distribution of the pore system within the two-dimensional images is fractal, then the $N(\delta)$ and the δ satisfy the relation:

$$N(\delta) \propto \delta^{-D} \tag{8.4}$$

where D is the box counting dimension. Thus, for fractal objects a double-logarithmic plot of $N(\delta)$ against δ yields a straight line of a slope equal to $-D$ [18]. For every calibrated image a sequence of five grids of boxes was used where the box size δ was reduced by a factor 1/2 (δ = 100, 50, 25, 12, 6 μm).

Mercury porosimetry and fractal dimension. Mercury porosimetry used in petrophysics to characterize the pore volume distribution of rocks is based on the gradual injection of mercury into an evacuated pore network as an external pressure is applied. Assuming that the pores are bundles of cylindrical capillary tubes, the Washburn equation relates capillary pressure and capillary diameters:

$$P_c = -\frac{4Y\cos\theta}{d_c} \tag{8.5}$$

where P_c is the capillary pressure required to force mercury into the evacuated pore space, Y is the surface tension of mercury, θ is the contact angle between mercury and the capillary tube, and d_c is the diameter of a cylindrical capillary tube, which models the diameter of a tubular pore throat. The increasing capillary pressure is plotted against the mercury saturation in terms of the percentage of rock pore volume saturated by mercury, resulting in the injection curve. Being the approximation of the distribution of pore volume accessible by throats of given effective size [27]. Thus, (8.5) becomes a relation between the pore space volume (V_p) and the injection capillary pressure (P_c):

$$V_p \propto P_c \tag{8.6}$$

We can consider the pore system of the rock as the Menger sponge fractal model where the pore diameter is assigned to the size of solid cube (r_0) of which the fractal model is constructed from. If the Menger sponge is injected with mercury as the injection pressure is applied then with increasing pressure smaller and smaller pores are filled so the volume of injected mercury increase and the density of the sponge increase consequently. Therefore, (8.3) and the relation (8.6) can be integrated to give the following expression for pore space volume (V_p) in function of pore fractal dimension (D_p) and capillary pressure (P_c):

$$V_p \propto P_c^{3-D_p} \tag{8.7}$$

The fractal dimension of pore volume (D_p) can therefore be deduced from the slope of the linear log-log plot of pore volume V_p against P_c [1, 3].

A Micromeritics Autopore 9500 mercury porosimeter was used to measure pore volume distribution as a function of pressure from 3.03×10^{-3} to 138 MPa (0.44 to 20×10^3 psia) or pore-throat diameters from 0.0090 to 413 μm on air-dried sandstone samples of the range of weight from 4.34 to 7.11 g. Values for the surface tension of mercury of 0.485 N/m and a contact angle on rock of 130° were used with the Washburn equation (8.5), assuming system of cylindrical capillary tubes in the calculation. The mercury-injection curve was describe by 32 pairs of applied pressure and intruded volume values but the initial portion of the intrusion curve associated with surface defects in samples was not taken into account in calculations of fractal dimensions [9].

8.3 Results

Results of image analysis of pore system. Each sample is represented by a pair of images, the OM image and the FEGSM image. All of the images have approximately similar resolutions, from 0.45 μm/pixel for two of the FEGSM images and 0.43 μm/pixel for all OM images to 0.38 μm/pixel for another two FEGSM images. The former FEGSM images cover an area of approximately 997,000 μm^2 while the

latter ones include an area nearly of 715,000 μm^2 whereas the OM images span an area close to 240,000 μm^2.

For binary images created by identifying the pixels associated with the pore phase including the overall porosity (total porosity), the ratio of the pore phase area to the total image area was calculated. This ratio is termed *the total optical porosity* or TOP [5]. The values of the TOP estimated for the OM images are usually higher than the physically measured total porosities of the samples (Table 8.1). Merely one value of the TOP (28.64 %) is consistent with the total porosity of the sample (28.42 %). However, the TOP-s calculated for the FEGSM images mostly correspond to the measured total porosities. There is one value of the TOP (11.83 %) lower than the total porosity (20.36 %).

Generally, the total porosity (TOP) defined by the image analysis is dependent on the thin-section selection and the field of view under the microscope. In addition, the porosity values estimated for the images taken from the optical microscopy (OM) are determined by the penetrating power of epoxy impregnation and the overlapping phenomena, being a consequence of that the transmission light penetrating the entire 20–30 μm of the thin section displays blurred pore outlines in contact to transparent or translucent minerals [2, 4].

The calculations of the fractal dimensions using the box counting method have been performed for the total optical porosity (TOP). The linear log-log diagrams of the number of boxes $N(\delta)$ against the box sizes (δ) obtained for all the images yield the straight regression lines fitting to the data. Thus, the power-law relation is proved for the pore phases revealed within two-dimensional images of thin sections. The box-counting fractal dimensions for the OM images range from 1.320 to 1.538, whereas for the FEGSM images vary from 1.448 to 1.564. The range of the coefficients of determination is wider for the OM images (0.9953–0.9987) while for the FEGSM images is narrow from 0.9991 to 0.9999 (Table 8.1).

Fractal analysis of mercury porosimetry data. The calculations of the fractal dimensions of the pore volume basing on the mercury porosimetry data and using the Menger sponge fractal model have been carried out for the pore-throat diameters range from 91 to 0.0090 μm. The results of the fractal analysis for all the samples studied are summarized in Table 8.2.

For each sample the double-logarithmic injection curve of the cumulated pore volume against the cumulated injection pressure displays two linear components which can be fitted with piece-wise regression lines to estimate two different fractal dimensions [cf [17]]. For each linear element the regression line was fitted for as narrow as possible the range of the pore-throat diameters (cumulative pressures) and for as high as possible the coefficient of determination (R^2).

These two linear components representing two separate fractal elements appear in two distinct ranges of the pore-throat diameters (or cumulated injection pressures) considerably lesser than *the threshold pore-throat diameters* (11.32–45.37 μm) corresponding to *the threshold pressures* (64.81–525.66 kPa). The inflection point of the rapidly rising portion of the injection curve indicates *the threshold pressure* as the pressure at which mercury forms a connected pathway across the sample (*percolation backbone*), [1, 9, 10].

Table 8.2 The results of fractal analysis of pore volume based on mercury porosimetry data

		Sample	1	2	3	4	Min	Max
The first fractal element								
Fractal dimension D_1			2.956	2.981	2.950	2.974	2.950	2.981
Pore-throat diameter	min	μm	0.0090	0.0090	0.0090	0.0090	0.0090	0.0090
	max	μm	0.2984	0.0905	0.2987	0.0905	0.0905	0.2987
R^2			0.9153	0.9093	0.9183	0.9819	0.9093	0.9819
The second fractal element								
Fractal dimension D_2			2.777	2.900	2.419	2.201	2.201	2.900
Pore-throat diameter	min	μm	0.9024	0.1800	1.2061	1.2057	0.1800	1.2061
	max	μm	4.5367	1.7661	3.6412	3.6387	1.7661	4.5367
R^2			0.9925	0.9794	0.9915	0.9961	0.9794	0.9961
Threshold pore-throat diameter		μm	45.37	30.23	11.34	11.32	11.32	45.37
Threshold pressure		kPa	64.81	143.89	525.52	525.66	64.81	525.66

R^2—coefficient of determination

The first fractal element tied to the range of the smallest pore-throat diameters (0.0090–0.2987 μm) is characterized by the fractal dimensions (D_1) varying from 2.950 to 2.981, whereas the fractal dimensions (D_2) for the second fractal element linked to the range of the greater pore-throat diameters (0.1800–4.5367 μm) extend from 2.201 to 2.900. The values of the coefficients of determination (R^2) are different for each linear unit 0.9093–0.9819 and 0.9794–0.9961, respectively (Table 8.2).

The two-section fractal distribution of pore-space volume identified by two different fractal dimensions within two separate ranges of the pore-throat diameters implies that the pore space is the multifractal pattern at two levels of scrutiny (ranges of scale or ranges of the pore-throat diameters). The first fractal exhibited at the highest values of the injection pressures (the smallest diameters) is referred to as *the textural fractal*, whereas the second fractal manifested at the lower values of the injection pressures (the greater diameters) is labeled as *the structural fractal* [11].

The following inference is based on the results of the research of Krohn and Thompson [14] suggesting that the microvolumes of the pore space of sandstones exhibit the fractal structures. Therefore the textural fractal dimension (D_1) can be considered as controlling the distribution of volume of the smallest pore-throat (necks). The assumption that the textural fractal dimension (D_1) characterizes the overall pore-throat network in studied sample provides a device to set apart the distribution of the pore-throat volume (only necks) from the distribution of the pore-space volume (pores and necks). The extrapolation of the regression line fitted to the included data points into all known cumulative injection pressures gives the cumulative distribution of the pore-throat volume which is consecutively normalized by assigning the zero value of the volume to the threshold pressure (threshold diameter). The difference between the cumulative distribution of the pore-space volume and the pore-throat volume gives the cumulative distribution of pore volumes. This method of the partition of the distribution of the pore-space volume was introduced by Such and Lesniak [23].

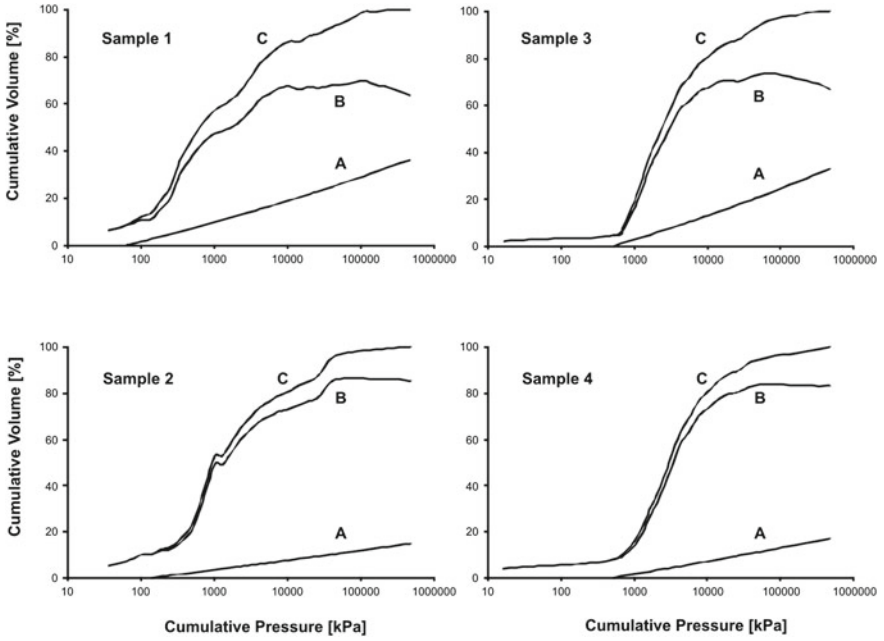

Fig. 8.1 The cumulative distributions of the pore-throat volume (A), the pore volume (B), and the pore-space volume (C) for studied samples

The distributions of the pore-throat volumes depend on the value of the textural fractal dimensions (D_1). The highest values of the fractal dimensions D_1 (2.974 and 2.981), typical of the narrow ranges of the pore-throat diameters (0.0090–0.0905 μm), result in the gradual distributions of the pore-throat volume in contrast to the steeper distributions determined by the lower values of the fractal dimensions D_1 (2.950 and 2.956) which characterize the wider range of the pore-throats (0.0090–0.2987 μm) (Figure 8.1).

8.4 Conclusions

The application of fractal geometry to studying the pore space in sandstones has been demonstrated for two different data sets (generated by mercury porosimetry and binary images) using two different methods.

The measurements of the fractal dimensions applying mercury porosimetry are based on the Menger sponge fractal model and indicate that the pore space is a bifractal pattern within two distinct ranges of the pore-throat diameters (0.0090–0.2987 μm) and (0.1800–4.5367 μm). The assumption that the textural fractal dimensions identified for the ranges of the smaller pore-throat diameters (0.0090–0.2987 μm) characterize the overall pore-throat network in the sandstones yields

a device making possible partitioning the cumulative distribution of the pore-space volume into the pore-throat volume and pore volume cumulative distributions (Figure 8.1).

The measurements of the fractal dimensions using the box counting method have been carried out for the two-dimensional images of thin sections of the sandstones which had been processed to extract the pore phase. The box-counting fractal dimensions (1.320–1.564) evaluated for the total optical porosity (45,000–281,000 μm^2) are different from those obtained for the mercury porosimetry data (2.201–2.981). Assuming that the sandstones studied are isotropic structures, the box-counting dimensions may be increased by a unity to obtain the corresponding fractal dimension of the pore volume in 3D [15]. The new values of the fractal dimensions (2.320–2.564) calculated in this way are included within the range of the fractal dimensions found for mercury porosimetry data. All values of the fractal dimensions computed in this study for the pore volume correspond to those found by Krohn and Thompson [14], Hansen and Skjetorp [6] and Pérez Bernal and Bello López [19]. The two methods applied indicate that the pore space of the sandstones studied is fractal, and the more the fractal dimensions approach a value of 3 the more complex is the pore volume.

Acknowledgments The FEGSM examinations were conducted at the Laboratory of Field Emission Scanning Electron Microscopy and Microanalysis of the Institute of Geological Sciences of the Jagiellonian University. This work was financed by the AGH-UST (statutory grant No. 11.11.140.320).

References

1. R.F. Angulo, V. Alvarado, H. Gonzalez, Fractal dimensions from mercury intrusion capillary tests. SPE **23695**, 255–263 (1992)
2. F.S. Anselmetti, S. Luthi, G.P. Eberli, Quantitative characterization of carbonate pore systems by digital image analysis. AAPG Bull. **82**(10), 1815–1836 (1998)
3. F. Bartoli, N.R.A. Bird, V. Gomendy, H. Vivier, S. Niquet, The relation between silty soil structures and their mercury porosimetry curve counterparts: fractals and percolation. Eur. J. Soil. Sci. **50**, 9–22 (1999)
4. R. Ehrlich, S.J. Crabtree, S.K. Kennedy, R.L. Cannon, Petrographic image analysis I, analysis of reservoir pore complexes. J. Sediment. Petrology **54**(4), 1365–1378 (1984)
5. R. Ehrlich, S.J. Crabtree, K.O. Horkowitz, J.P. Horkowitz, Petrography and reservoir physics I: objective classification of reservoir porosity. AAPG Bull. **75**(10), 1547–1562 (1991)
6. J.P. Hansen, A.T. Skjeltorp, Fractal pore space and rock permeability implications. Phys. Rev. B **38**(4), 2635–2638 (1988)
7. J.P. Hyslip, L.E. Vallejo, Fractal analysis of the roughness and size distribution of granular materials. Eng. Geol. **48**, 231–244 (1997)
8. A.J. Katz, A.H. Thompson, Fractal sandstone pores: implications for conductivity and pore formation. Phys. Rev. Lett. **54**(12), 1325–1328 (1985)
9. A.J. Katz, A.H. Thompson, Quantitative prediction of permeability in porous rock. Phys. Rev. B **34**(11), 8179–8181 (1986)
10. A.J. Katz, A.H. Thompson, Prediction of rock electrical conductivity from mercury injection measurements. J. Geophys. Res. **92**, 599–607 (1987)

11. B.H. Kaye, Image analysis techniques for characterizing fractal structures, in *The Fractal Approach to Heterogeneous Chemistry*, ed. by D. Avnir (Wiley, Chichester, 1989), pp. 55–66
12. C.E. Krohn, Sandstone fractal and Euclidean pore volume distributions. J. Geophys. Res. **93**(B4), 3286–3296 (1988)
13. C.E. Krohn, Fractal measurements of sandstones, shales, and carbonates. J. Geophys. Res. **93**(B4), 3297–3305 (1988)
14. C.E. Krohn, A.H. Thompson, Fractal sandstone pores: automated measurements using scanning-electron-microscope images. Phys. Rev. B **33**(9), 6366–6374 (1986)
15. B.B. Mandelbrot, *The Fractal Geometry of Nature* (Freeman, New York, 1983)
16. C.A. McCreesh, R. Ehrlich, S.J. Crabtree, Petrography and reservoir physics II: relating thin section porosity to capillary pressure, the association between pore types and throat size. AAPG Bull. **75**(10), 1563–1578 (1991)
17. J.D. Orford, W.B. Whalley, The use of the fractal dimension to quantify the morphology of irregular-shaped particles. Sedimentology **30**, 655–668 (1983)
18. H.O. Peitgen, H. Jürgens, D. Saupe, *Chaos and Fractals: New Frontiers of Science* (Springer, New York, 1992)
19. J.L. Pérez Bernal, M.A. Bello López, The fractal dimension of stone pore surface as weathering descriptor. Appl. Surface Sci. **161**, 47–53 (2000)
20. P. Pfeifer, D. Avnir, Chemistry in noninteger dimensions between two and three. I. Fractal theory of heterogeneous surfaces. Jour. Chem. Phys. **79**(7), 3558–3565 (1983)
21. P. Pfeifer, M. Obert, Fractals: basic concepts and terminology, in *The Fractal Approach to Heterogeneous Chemistry*, ed. by D. Avnir (Wiley, Chichester, 1989), pp. 11–43
22. E.D. Pittman, Relationship of porosity and permeability to various parameters derived from mercury injection-capillary pressure curves for sandstone. AAPG Bull. **76**(2), 191–198 (1992)
23. P. Such, G. Lesniak, Study of pore space parameters of rocks. Prace Instytutu Gornictwa Naftowego i Gazownictwa **119**, 3–63 (2003) (summary in English)
24. A.H. Thompson, A.J. Katz, C.E. Krohn, The microgeometry and transport properties of sedimentary rock. Adv. Phys. **36**(5), 625–694 (1987)
25. D.L. Turcotte, *Fractals and Chaos in Geology and Geophysics* (Cambridge University Press, Cambridge, 1992)
26. D.L. Turcotte, J. Huang, Fractal distribution in geology, scale invariance, and deterministic chaos, in *Fractals in the Earth Sciences*, ed. by C.C. Barton, P.R. La Pointe (Plenum Press, New York, 1995), pp. 1–40
27. C.L. Vavra, J.G. Kaldi, R.M. Sneider, Geological applications of capillary pressure: a review. AAPG Bull. **76**(6), 840–850 (1992)